A new corrosion mechanism for X100 pipeline steel under oil-covered chloride droplets

Hongxing Liang,, *** Jing Liu,* Rebecca Filardo Schaller,* and Edouard Asselin.**

** Department of Materials Engineering, The University of British Columbia, Vancouver, BC, Canada.*

ARTICLE INFO (THIS STYLE IS ARTICLE AND ABSTRACT HEADING)

Article history:

Received Day Month Year (This style is Article History and Keywords)
Accepted Day Month Year
Available Day Month Year

Keywords:

A. Steel
B. Pipelines
C. Pitting
D. Uniform corrosion

***Corresponding author: Hongxing Liang, telephone +001 6047739849; Department of Materials Engineering, The University of British Columbia, Frank Forward Building, 309-6350 Stores Road, Vancouver, BC, V6T 1Z4, Canada, email: (hongxingliang314@gmail.com).

"THIS IS A PREPRINT. THIS ARTICLE WAS PUBLISHED IN <Corrosion>.
DOI: <https://doi.org/10.5006/2804>"

ABSTRACT

A 0.17 mM NaCl droplet on X100 pipeline steel covered by paraffin oil is used to simulate the corrosive environment encountered in heavy oil or bitumen pipelines. The development of corrosion under the droplet was monitored and explored in two stages. In the initial stage (1 h), the distribution of corrosion pits was heterogeneous with one area under the droplet presenting a higher pit density. As the corrosion proceeded (24 h), the localized corrosion in the area under the droplet with the higher pit density switched to general corrosion, while the other region of the droplet continued to pit. The mechanisms driving this new distinctive corrosion form developed beneath an underoil salty droplet on X100 pipeline steel are explained.

INTRODUCTION

Bitumen production is expected to increase over the next decade owing to the technological advances in processing and the increased global demand for oil.[1] The rapid expansion of the bitumen industry may result in challenges with respect to the safe transportation of bitumen within steel pipelines. Current technology such as naphtha-froth treatment cannot completely remove all the water from bitumen and the remaining water is present as droplets within the bitumen.[2] In addition, the droplets associated with bitumen carry chloride salts, such as sodium chloride (NaCl), that originate from marine sediments.[3] Bitumen on its own is too thick to flow, so it must be diluted in order to be effectively pumped through a pipeline.[2] The droplets enter the pipeline with the diluted bitumen and some droplets may accumulate on pipeline surfaces under certain circumstances, such as changes in flow patterns[4] and overbends.[5] Consequently, the droplets can accumulate on the inner surface of the pipeline and may cause internal corrosion of pipeline steel.[6]

Extensive research has been conducted on the corrosion behavior of steel under salt-containing droplets in marine atmospheres.[7-13] The classic Evans' drop experiment, provides insight into the mechanism of droplet corrosion of steels.[7] According to the Evans model, the corrosion rate distribution in a salt-containing droplet is heterogeneous with the droplet center behaving as an anode and the cathodic reaction occurring at the droplet edge due to differential diffusion of oxygen (O_2).[7] Furthermore, the solution at the edge of the droplet will become alkaline through O_2 reduction and the central part will develop an acidic pH due to the hydrolysis of the ferrous ion (Fe^{2+}).[7] Droplet spreading and formation of microdroplets can also exacerbate the alkaline pH at the droplet edge, again through O_2 reduction.[14] Evans' results were validated by several studies.[8, 9, 15] However, the Evans model was not applicable for a small droplet where oxygen depletion at the drop center did not occur. Li *et al.* concluded that the corroded area (anode) for carbon steel under small NaCl droplets (45−200 μm) always preferably appeared within crevices between the matrix alloy and any inclusions that may be present *i.e.* not in the central part of a droplet.[10]

In contrast to droplets open to humid air, if a salt-containing droplet is covered by an oil phase, the oil phase limits the oxygen supply which can significantly alter the droplet corrosion morphology. In this case O_2 reduction becomes the rate limiting step in corrosion of the steel as it is governed by the cathodic reaction rate.[16] Furthermore, it is reported that droplet evaporation is significantly reduced when it is covered by an oil phase.[17] In atmospheric exposures, droplet stability and salt concentration will be governed by the equilibrium deliquescence of the salt in the exposure humidity.[11, 18] However, as indicated by Brumshtein *et al.*,[19] a 0.55 μL water droplet covered by paraffin oil maintained a stable shape for 14 days at 22 °C and at an external humidity of 65–75%. Thus, a distinct difference in the corrosion behavior of steel may occur when the droplet is covered by an oil phase that limits oxygen diffusion, evaporation, and possibly droplet spreading. Such a scenario is expected in practical pipeline applications. Consequently, the pitting corrosion and longer term corrosion of X100 pipeline steel were investigated underneath a salt-containing droplet covered by paraffin oil.

Scanning electron microscopy (SEM), Raman spectroscopy, and X-ray photoelectron spectroscopy (XPS) were used to identify pH specific corrosion product phases. Additionally, the characterization at different stages of corrosion evolution was carried out to determine the underoil droplet effect on the resultant corrosion morphology. The data collected here can help better understand droplet corrosion in diluted bitumen pipelines.

Experimental

Materials and solutions

The chemical composition of the X100 pipeline steel examined in this work is provided in Table 1. Samples with dimensions of 10 × 10 × 6 mm were cut from a 6 mm thick X100 pipeline steel sheet. The samples were sequentially ground by SiC papers of 120, 320, 600, and 1,200 grit, and then rinsed ultrasonically with reagent-grade alcohol for 10 min. The samples were then dried under warm air. Deionized (DI) water and NaCl (Cryst./Certified ACS) were used to prepare the droplet

solutions. The salt-containing droplets in diluted bitumen pipelines have low chloride contents compared with the water phase in other conventional crude oil pipelines.[5] Droplets containing 0.17 mM NaCl dissolved in DI water were chosen in this study, which simulate droplets formed in diluted bitumen pipelines.[3, 5] The initial oxygen concentration inside the NaCl solution was measured by an Extech 407510 oxygen meter (Extech Instruments), and the average value was 0.269 mmol L^{-1}.

Corrosion under a droplet

A schematic for the deposition of the NaCl droplet under paraffin oil is shown in Figure 1. The temperature of the paraffin oil (VWR analytical grade) was maintained at 23 °C in a jacketed cell connected to a water bath with an accuracy of ±1 °C. A 2 µL NaCl droplet was deposited on the polished sample surface. The samples coupled with the droplets were placed in a second jacketed cell. A syringe was used to fill paraffin oil into the jacketed cell to cover the droplet and sample completely with an oil film thickness of 40 mm. The exposure times were 1 h and 24 h, respectively. The exposure temperature was controlled at 23 °C. After exposure, sample surfaces were cleaned using reagent-grade alcohol to remove the droplet and the residual paraffin oil on the sample surface. A procedure based on ASTM G1-03 was used on the surface of select samples to remove the corrosion products.[20] This standard provides the method for removing corrosion products without the significant removal of the steel matrix.[20] The composition of the descaling solution was hydrochloric acid (HCl, ACS reagent) (volume ratio 1:1) + 0.025 M methenamine ($(CH_2)_6N_4$, Anachemia). Once the corrosion products were removed, the samples were cleaned with reagent-grade alcohol and dried under warm air. Droplet experiments were repeated a minimum of three times to ensure consistency.

Monitoring the droplet pH

The droplet pH was measured using a wide range pH indicator (Ricca Chemical Company). To establish reference colors, the pH indicator was added to buffer solutions with pH 1, 4, 5, 7, and 9. The reference colors were then recorded by a digital camera. Subsequently, the pH indicator was added to 0.17 mM NaCl solution and a droplet of 2 µl of this solution was dropped on the sample. Paraffin oil was used to cover the droplet. Finally, a digital camera monitored the images after exposure for 24 h. The pH measurements were repeated at least three times to ensure reliability.

Surface-analysis measurements

A field emission scanning electron microscope (SEM, Zeiss Σigma) coupled with Energy dispersive X-ray spectrometry (EDS) was employed to characterize surface morphology before and after etching the samples. The accelerating voltage during SEM measurements was 20 kV. Raman spectroscopy was undertaken using a LabRam HR (by Horiba Scientific) with the LabSpec 6 software. Prior to each set of experiments, the Raman shift was calibrated by the 520.7 cm^{-1} band of a Si target. The samples were excited with the 441.6 nm line from an air-cooled He-Cd laser. The range 200−1,100 cm^{-1} with a 60 s collection time was selected to measure the spectra. Both SEM and Raman measurements were repeated at three different positions in the selected zones to ensure consistent results.

XPS measurements were conducted on an Omicron & Leybold MAX200 machine with a monochromated Al Kα source (1486.6 eV). The absolute binding energies were calibrated by the C 1s line of adventitious carbon at 284.8 eV binding energy. The XPS data were fitted using the XPSPEAK Version 4.1 software. The three-dimensional corrosion attack underneath corrosion products was measured on samples cleaned according to ASTM G1-03 by a surface profilometer (Dektak XT, Bruker).

Results

Initial stage of corrosion (1h)

SEM images showing the morphologies of the sample beneath the NaCl droplet for 1 h are given in Figure 2(a). The distribution of corrosion products was relatively homogeneous. After the removal of the corrosion products (Figure 2(b,c, and d)), only pitting corrosion can be seen. As shown in Figure 2(d), some pits distributed in the central region of the droplet. In addition, Figure 2(b) showed more corrosion pits with respect to Figure 2(c). The pit density in Figure 2(b) is 9600 pits per cm^2, whereas the pit density of Figure 2(c) is 4000 pits per cm^2.

The crystal structures frequently identified in the corrosion products of steel include hematite (α-Fe_2O_3), maghemite (γ-Fe_2O_3), magnetite (Fe_3O_4), ferrihydrite ($Fe_5HO_8{\cdot}4H_2O$), goethite (α-FeOOH), akaganeite (β-FeOOH), lepidocrocite (γ-FeOOH), and feroxyhyte (δ-FeOOH).[21] The morphology of the corrosion products, which can sometimes indicate the nature of Fe crystals, was identified by SEM. These crystal structures were further, and separately, analysed by Raman spectroscopy. High-magnification SEM images showing the crystal structures of the corrosion products present in Figure 2(a) are provided in Figure 3. Hematite with hexagonal platelets is observed in Figure 3(a).[22] As stated in the literature,[21, 23] the fine plate structures (flowery structures) observed in Figure 3(b) are attributed to lepidocrocite. A Raman spectrum of the corrosion products in Figure 2(a) is displayed in Figure 4. The spectrum presents two peaks at 217 and 284 cm^{-1}, which belong to that of lepidocrocite.[24-27] The peaks at 502 and 602 cm^{-1} indicate the presence of hematite.[25, 27, 28] The peak at 670 cm^{-1} may be attributed to either hematite or the coexistence of hematite and magnetite.[25] Table 2 lists the peak positions of Raman spectra corresponding to the crystal structures present in the corrosion products. Owing to the limited size of the area observed by SEM and Raman spectra, there may be other crystal structures present in the corrosion products, however, those that were observed likely represent the most abundant.

Longer term corrosion (24h)

Figure 5 presents the SEM images of the corrosion morphology of a sample beneath a droplet after 24 h of exposure. Two distinct regions were labeled with numbers 1 and 2 in Figure 5(a). Region 2 displays more significant corrosion products than region 1. After the removal of the corrosion products, Figure 5(d) suggests again that there were two distinct corrosion morphologies across these regions. The inserted SEM image in Figure 5(d) clearly demonstrates that the right region (active region) experienced more severe corrosion with respect to the left region (inactive region). Between 1 and 24 h of exposure, the corrosion mode switched from the initial pitting corrosion to uniform corrosion in the active region. It should be noted that the location of the active regions is random and dependent on the stochastic nature of pitting and the subsequent pit density, i.e. it is not always necessarily on the right side of specimens. The active region was placed on the right side of the images for consistency.

The three-dimensional morphology of the corrosion attack under the corrosion products for the specimen under a 2 µL NaCl droplet for 24 h was characterized in order to further confirm the establishment of the active and inactive regions. As shown in Figure 6, the corrosion of the active region is heterogeneous with the edge presenting the deepest attack. The average corrosion depth in the active region is 1.17 µm, while only some pits can be observed in the inactive region. It is obvious that the entire active region experienced severe corrosion attack with respect to the inactive region.

The crystal structures of the corrosion products formed across different regions in Figure 5(a) are given in Figure 7. In region 1 of Figure 5(a), the rose-type flowers (Figure 7(a)) with bent and folded lamellae crystal structures are lepidocrocite.[29] Hematite with

hexagonal platelets (Figure 7(b)) was observed in region 1 of Figure 5(a).[22] The fine plate structures (flowery structures) in Figure 7(c) are also lepidocrocite.[21, 23] In Figure 7(d), the crystal structures show cross-linked lamellae with two ends fanning out, which correspond to goethite.[22] Hexagonal hematite (Figure 7(e)) and lepidocrocite showing the fine plate structure and the rose-type flower structure (Figure 7(f)) are also seen in region 3 of Figure 5(a). The circular plates with the diameters ranging from 100 nm to 300 nm are hematite (Figure 7(f)).[29, 30] Different crystal structures were observed to form and were correlated to their location under the droplet.

The Raman spectra of the regions marked in Figure 5(a) are given in Figure 8. The Raman spectrum for region 1 (Figure 8(a)) shows the peaks at 217 and 284 cm^{-1} which suggest the formation lepidocrocite (see Table 2). The peaks at 401, 502 and 602 cm^{-1} were assigned to hematite. The peak at 670 cm^{-1} may be assigned to either hematite or the coexistence of hematite and magnetite. The peaks at 217 and 713 cm^{-1} in Figure 8(b) are attributed to lepidocrocite. The peaks at 300 and 993 cm^{-1} (Figure 8(b)) are attributed goethite. The presence of hematite in region 2 can be suggested by the peaks at 401, 502, and 602 cm^{-1} in Figure 8(c).

Figure 9 presents the high-resolution XPS spectra of the specimens under the NaCl droplet for 24 h. Fe, O, C, and Cl elements were found in the corrosion products. The broad complex XPS plot of Fe 2p is fitted with three peaks at 710.5, 712.1, and 714.0 eV, which are assigned to Fe^{2+}, Fe^{3+} and satellite peaks, respectively.[31] The XPS peak for O 1s is fitted by three sub-peaks. The peaks at 529.9, 531.3, and 532.8 eV are attributed to O^{2-}, OH^-, and H_2O, respectively.[32] The peak at 198.9 eV reveals the presence of Cl^- in the corrosion products. [33]

The pH of the different regions under the droplet was also recorded with a digital camera to study the pH separation under the droplet. After 1 h, the pH separation was not established and the whole area presented a pH of approximately 7. After 24 h (Figure 10), a qualitative comparison between droplet colors and reference colors implies that the active region had a pH of 4−5 and the inactive region displayed a pH of approximately 9. Figure 10 (h and i) displays the active and inactive corrosion regimes with and without the presence of pH indicator during the exposure period, suggesting this phenomenon is due to the conditions established in the underoil exposure and not the interference of pH indicator. This is corroborated by Azmat *et al.* who successfully used similar methods to measure the pH evolution of a droplet deposited on Zn in a marine environment.[34]

Discussion

The sulfur compounds and organic acids present in diluted bitumen do not normally lead to steel corrosion at the normal operating temperatures of pipelines.[5] The NaCl droplet covered by paraffin oil (or other oil products) represents one possible corrosive scenario for these pipelines. Based on the observed morphology, the development of corrosion under such a droplet is divided into two stages: stochastic pitting corrosion until a significant pH change in the acid direction is affected, followed by uniform corrosion in the active and low pH region. This is different from the classic Evans' drop experiment where the cathodic reaction occurs at the droplet edge and the droplet center behaves as an anode due to the oxygen deficit in the droplet center.[7] To confirm that the observed morphology was a result of the oil covering, an experiment with a 2 µL 0.17 mM NaCl droplet in a controlled humidity environment without oil covering at 23 °C was also performed (supplementary information). The corrosion morphology of X100 pipeline steel under these conditions was quite similar to that first observed by Evans.[7] However, Evans' and other similar studies on droplet corrosion in a humid environment cannot be applied to the particular case of droplet corrosion with an oil covering. A new distinctive corrosion mechanism considering both the corrosion initiation and longer term corrosion needs to be proposed.

The initial stage of corrosion (1 h)

During the initial stage (1 h), the distribution of corrosion products and locally active sites was relatively homogeneous (Figure 2(a)). As shown in Figure 2(d), pits were concentrated in the center region of the droplet. In addition, Figure 2(b) showed a higher density of corrosion pits with respect to Figure 2(c). Figure 11(a) provides a schematic model illustrating the corrosion initiation of the specimen under a droplet covered by paraffin oil. The dissolution sites behaved as anodes, and the iron in anodic areas was oxidized to Fe^{2+}. The areas surrounding the anodes served as cathodes.

Anodic dissolution of the metal (1) and cathodic O_2 reduction (2) proceeded under the droplet at the early stages:[35]

$$Fe = Fe^{2+} + 2e^- \quad (1)$$

$$H_2O + 1/2O_2 + 2e^- = 2OH^- \quad (2)$$

Calculations of metal loss through charge balance (using the initially measured oxygen concentration and assuming zero oxygen diffusion through the paraffin oil) showed that oxygen would have been depleted in the droplet within the first hour. Further, replenishment of oxygen in the droplet, through the oil, would have been significantly reduced by the slow diffusion rate of oxygen through oil.[36, 37] As a result, hydrogen evolution likely became dominant over longer time periods. Subsequently, the Fe^{2+} produced at the pits can lead to hydrolysis and H^+ production:[38]

$$Fe^{2+} + 2H_2O = Fe(OH)_2 + 2H^+ \quad (3)$$

Production of $Fe(OH)_2$ can also occur in alkaline regions according to:[9]

$$Fe^{2+} + 2OH^- = Fe(OH)_2 \quad (4)$$

Further consumption of oxygen would have occurred due to the oxidation of $Fe(OH)_2$, which is not stable in oxygenated aqueous solutions[39]:

$$2Fe(OH)_2 + 1/2O_2 = 2FeOOH + H_2O \quad (5)$$

$$2Fe(OH)_2 + 1/2O_2 = Fe_2O_3 + 2H_2O \quad (6)$$

The XPS data presented in Figure 9 reveal the presence of Fe^{2+}, Fe^{3+}, OH^-, and O^{2-} in the corrosion products, which corroborates reactions 1−6. As shown in Figure 3 and 4, lepidocrocite with fine plate structures and hexagonal hematite can be identified in the corrosion products. Dengfeng *et al*.[22] proposed that hexagonal hematite platelets tend to form in aqueous solutions with enough OH^- and the circular hematite platelets can form in low pH solutions. It is inferred that the cathodic reaction in this stage led to the pH rise. Thus hexagonal hematite formed around the cathodes during this stage.

Longer term corrosion (24 h)

In the longer term corrosion experiments (24 h), the entire droplet area was split into an inactive and an active region (Figure 5(d) and 6). Han *et al.* investigated the electrochemical corrosion behavior of steel under a deoxygenated droplet covered by paraffin oil, and they reported that the formation of corrosion products "passivated" the steel after 4 h.[5] However, in the present study, it is found that the corrosion sites in the active region led to hydrolysis and local decrease in pH of the solution (Figure 10(f)). As O_2 diffusion was limited across

the entire droplet the pH was dependent on the location and density of pits due to stochastic pit initiation and stabilization. Additionally, Han *et al.* did not form a "true" droplet as the chloride solution on the surface of the steel was confined within a capillary tube. This is in contrast to the present work where the droplet was constrained only by the paraffin.

Figure 11(b) provides a mechanistic model illustrating the longer-term corrosion of the specimen under a droplet covered by paraffin oil. During the initiation stage, pits were distributed in the central part of the area under the droplet. However, more pits were initiated on the right side of Figure 2(d), where the active region eventually took hold. More pits in the active region induced a difference in the concentration of dissolved metal ions which led to hydrolysis and the pH differential. The resulting corrosion products of the active region were usually thicker and denser than on the inactive region (Figure 5(b) and (c)). The continuous and more rapid generation of Fe^{2+}, and its subsequent hydrolysis, (reaction 3) led to a pH drop of the solution on the active region, as given in Figure 10. The pH drop resulted in the transformation of the solution chemistry of the active area to a slightly more aggressive one. The aggressive solution, of pH 4-5, over the corroded region favoured sustained active dissolution. Consequently, the corrosion of the pits tended to horizontally propagate and this led to the formation of the active region, as demonstrated in Figure 5(d).[40] The sustained pitting corrosion in the active region combined with the limited supply of O_2 and lack of pH neutralization resulted in a switch to a uniform corrosion mode. In the inactive region, the pH was approximately 9 after 24 h of exposure. It is inferred that the predominant reaction in the inactive region was the cathodic reaction (reaction 2 or hydrogen evolution) which led to the pH rise. The cathodic reaction also accepted the electrons from the active region (reaction 1) to achieve charge balance. It is reported that corrosion rates of X100 pipeline steel decreased with increasing pH.[41] Consequently, only pitting corrosion can be observed in the inactive region (Figure 6). In summary, due to the pH evolution within the droplet, the pitting corrosion in the active region switched to uniform corrosion, while the inactive region maintained the smaller number of pits that had initiated during short term corrosion. The inactive region increasingly became cathodic with respect to the active region. The continued corrosion in the active region is governed by the pH differential, the hydrolysis and H^+ production, and the diffusion of H^+ to the cathodic (inactive) region. In contrast to the traditionally observed Evans droplet, governed by differential aeration, the corrosion attack for an exposure of a salty droplet underoil is based on the formation of a corrosion cell with an active and inactive region due to the stochastic nature of the initial pit density established at short exposure times.

As stated in the literature,[21] the two phases always detected in steel corrosion products are lepidocrocite and goethite. Other phases such as magnetite or maghemite and hematite can also be identified. Wang *et al.*[42] claimed that lepidocrocite and hematite formed first. Lepidocrocite then transformed into goethite. This was established by Ma *et al.*,[43] who reported that a pH drop facilitates the transformation of lepidocrocite to goethite by accelerating the dissolution of lepidocrocite. In the present study, when the steel was exposed to the droplet for 1 h, only hexagonal hematite and flowery lepidocrocite were observed (Figure 3). After 24 h, circular hematite and goethite were also seen in the active region (Figure 7(e) and (f)). Therefore, for the droplet covered by paraffin oil, it is likely that the hexagonal hematite and flowery lepidocrocite formed first, and that some of the lepidocrocite was transformed into goethite in the active region, which is consistent with the pH drop observed in the active region. As mentioned before, the circular hematite platelets can form in low pH solutions. As the corrosion proceeded, the active region decreased in pH due to hydrolysis, which gave rise to the formation of circular hematite. Thus the detection of goethite and circular hematite in the active region further confirms the pH evolution of the droplet covered by paraffin oil.

The most common oxyhydroxides of iron are lepidocrocite, goethite, akaganeite and feroxyhyte. In fact, the formation of lepidocrocite takes place on rusted surfaces that are easily accessible to oxygen, while akaganeite typically forms within a rust layer, where the O_2 supply from the atmosphere is inhibited.[44] In addition, a high Cl^- content (at least 2–3 M) is another fundamental factor for the formation of akaganeite.[44, 45] Akaganeite was not detected in this study, due to the low Cl^- content in the droplet. Also, feroxyhyte was not found in any of the regions under the NaCl droplet. It has been demonstrated that feroxyhyte typically forms in the presence of bubbling O_2 and at strong alkalinity.[46] In the present study, the O_2 in the droplet was insufficient for the formation of feroxyhyte. Consequently, among the oxyhydroxides, only lepidocrocite and goethite were identified in this study.

Conclusions

- After 1 h exposure under an NaCl droplet covered by paraffin oil, only pitting corrosion was observed in the central part of the droplet on X100 pipeline steel. The distribution of the corrosion pits was inhomogeneous with one region under the droplet showing a higher pit density.

- As corrosion progressed, the thicker and denser corrosion products, associated with more severe corrosion damage, were observed in the area under the droplet with the initial higher pit density. The active dissolution and increased hydrolysis above the higher pit density regions led to local formation of aggressive solutions (lower pH) and sustained the active dissolution. The cathodic reaction in the inactive region led to a measurable pH rise and a clear definition between the active and inactive regions. The pitting corrosion in the active region had switched to uniform corrosion due to the more aggressive conditions, while the inactive region still presented the pits formed during the initial stages of corrosion.

- The corrosion sequence and subsequent corrosion cell formed from a salty droplet in an underoil exposure is distinct from the traditional Evans droplet in that the active corrosion is governed by the initial stochastic nature of pit density rather than differential aeration of oxygen. The resultant corrosion morphology can be applied to better understand corrosion in susceptibility in bitumen pipelines.

Acknowledgments

The financial support from the Natural Sciences and Engineering Research Council of Canada (NSERC) is acknowledged by the authors. Hongxing Liang expresses his gratitude to the China Scholarship Council for their financial support of his doctoral studies in Canada.

References

1. E.W. Allen, *Journal of Environmental Engineering and Science* 7, 2 (2008): p. 123-138.
2. J. Wu, T. Dabros, *Energy Fuels* 26, 2 (2012): p. 1002-1008.
3. H. Kaur, P. Eaton, M. Gray, *Pet. Sci. Technol.* 30, 10 (2012): p. 993-1003.
4. J. Cai, C. Li, X. Tang, F. Ayello, S. Richter, S. Nesic, *Chem. Eng. Sci.* 73, (2012): p. 334-344.
5. D. Han, R. Jiang, Y. Cheng, *Electrochim. Acta* 114, (2013): p. 403-408.
6. R. Jiang, Y. Cheng, *Electrochem. Commun.* 35, (2013): p. 8-11.

7. U.R. Evans, *The Corrosion and the Oxidation of Metals*, St. Martins Press, New York, 1960.
8. C. Chen, F. Mansfeld, *Corros. Sci.* 39, 2 (1997): p. 409-413.
9. S. Li, L. Hihara, *Electrochem. Commun.* 18, (2012): p. 48-50.
10. S. Li, L. Hihara, *J. Electrochem. Soc.* 159, 4 (2012): p. 147-154.
11. E. Schindelholz, B. Risteen, R. Kelly, *J. Electrochem. Soc.* 161, 10 (2014): p. 450-459.
12. E. Schindelholz, B. Risteen, R. Kelly, *J. Electrochem. Soc.* 161, 10 (2014): p. 460-470.
13. S. Street, A. Cook, H. Mohammed-Ali, T. Rayment, A. Davenport, "The effect of deposition conditions on atmospheric pitting corrosion location under Evans droplets on 304L stainless steel," *Corrosion*, in press (2017): doi: 10.5006/2614.
14. T. Tsuru, K.-I. Tamiya, A. Nishikata, *Electrochim. Acta* 49, 17-18 (2004): p. 2709-2715.
15. T. Muster, A. Bradbury, A. Trinchi, I. Cole, T. Markley, D. Lau, S. Dligatch, A. Bendavid, P. Martin, *Electrochim. Acta* 56, 4 (2011): p. 1866-1873.
16. C. Leygraf, I.O. Wallinder, J. Tidblad, T. Graedel, Atmospheric Corrosion, John Wiley & Sons, 2016.
17. D. Langevin, Adv. *Colloid Interface Sci.* 88, 1–2 (2000): p. 209-222.
18. S. Li, L. Hihara, *Corrosion Engineering, Science and Technology* 45, 1 (2010): p. 49-56.
19. B. Brumshtein, H.M. Greenblatt, A.H. Futerman, I. Silman, J.L. Sussman, *J. Appl. Crystallogr.* 41, 5 (2008): p. 969-971.
20. ASTM G1, "Standard Practice for Preparing, Cleaning, and Evaluating Corrosion Test Specimens" (West Conshohocken, PA: ASTM International, 2011).
21. D. De la Fuente, I. Díaz, J. Simancas, B. Chico, M. Morcillo, *Corros. Sci.* 53, 2 (2011): p. 604-617.
22. D. Peng, S. Beysen, Q. Li, Y. Sun, L. Yang, *Particuology* 8, 4 (2010): p. 386-389.
23. M. Morcillo, R. Wolthuis, J. Alcántara, B. Chico, I. Díaz, D. de la Fuente, *Corrosion* 72, 8 (2016): p. 1044-1054.
24. S. Das, M.J. Hendry, *Chem. Geol.* 290, 3 (2011): p. 101-108.
25. A. Dumoulin, C. Trigance, D. Neff, E. Foy, P. Dillmann, V. L'Hostis, *Corros. Sci.* 52, 10 (2010): p. 3168-3179.
26. A.P. Lee, J. Webb, D.J. Macey, W. van Bronswijk, A.R. Savarese, G.C. de Witt, *JBIC Journal of Biological Inorganic Chemistry* 3, 6 (1998): p. 614-619.
27. M. Nieuwoudt, J. Comins, I. Cukrowski, *J. Raman Spectrosc.* 42, 6 (2011): p. 1335-1339.
28. M. Morcillo, B. Chico, J. Alcántara, I. Díaz, R. Wolthuis, D. de la Fuente, *J. Electrochem. Soc.* 163, 8 (2016): p. 426-439.
29. J. Alcántara, B. Chico, I. Díaz, D. de la Fuente, M. Morcillo, *Corros. Sci.* 97, (2015): p. 74-88.
30. P. Dillmann, F. Mazaudier, S. Hoerle, *Corros. Sci.* 46, 6 (2004): p. 1401-1429.
31. C.M. Grossi, D. Benavente, *Appl. Surf. Sci.* 384, (2016): p. 525-529.
32. Y. Li, Y.F. Cheng, *Appl. Surf. Sci.* 396, (2017): p. 144-153.
33. A. Zarrouk, B. Hammouti, T. Lakhlifi, M. Traisnel, H. Vezin, F. Bentiss, *Corros. Sci.* 90, (2015): p. 572-584.
34. N. Azmat, K. Ralston, B. Muddle, I. Cole, *Corros. Sci.* 53, 4 (2011): p. 1604-1615.
35. M. Morcillo, D. De la Fuente, I. Díaz, H. Cano, *Rev*. *Metal. Madrid* 47 (2011): p. 426.
36. Y.M. Stokes, *Mol. Reprod. Dev* 76, 12 (2009): p. 1178-1187.
37. J.M. Baltz, J.D. Biggers, *Mol. Reprod. Dev* 28, 4 (1991): p. 351-355.
38. T. Kushida, *ISIJ Int.* 43, 4 (2003): p. 470-474.
39. I.C. Thanos, *Journal of electroanalytical chemistry and interfacial electrochemistry* 210, 2 (1986): p. 259-264.
40. Y. Wang, G. Cheng, W. Wu, Q. Qiao, Y. Li, X. Li, *Appl. Surf. Sci.* 349, (2015): p. 746-756.
41. I.M. Gadala, A. Alfantazi, *Corros. Sci.* 82, (2014): p. 45-57.
42. Z. Wang, J. Liu, L. Wu, R. Han, Y. Sun, *Corros. Sci.* 67, (2013): p. 1-10.
43. Y. Ma, Y. Li, F. Wang, *Corros. Sci.* 51, 5 (2009): p. 997-1006.
44. K. Nomura, M. Tasaka, Y. Ujihira, *Corrosion* 44, 3 (1988): p. 131-135.
45. M. Morcillo, J. González-Calbet, J. Jiménez, I. Díaz, J. Alcántara, B. Chico, A. Mazarío-Fernández, A. Gómez-Herrero, I. Llorente, D. De la Fuente, *Corrosion* 71, 7 (2015): p. 872-886.
46. M. Gotić, S. Popović, S. Musić, *Mater. Lett.* 21, 3-4 (1994): p. 289-295.

FIGURE CAPTIONS

FIGURE 1. Schematic of the setup for droplet deposition and exposure under paraffin oil.

FIGURE 2. SEM secondary electron (SE) images of X100 pipeline steel specimen under a 2 µL 0.17 mM NaCl droplet beneath paraffin oil post 1 h exposure (a)and after removal of corrosion products (b, c, and d).

FIGURE 3. SEM SE images of the crystal structures of the corrosion products formed on the X100 pipeline steel specimen under a 2 µL 0.17 mM NaCl droplet exposed under paraffin oil for 1 h.

FIGURE 4. Raman spectrum of the corrosion products of the sample under a 2 µL 0.17 mM NaCl droplet exposed under paraffin oil for 1 h.

FIGURE 5. SEM SE images of the corrosion products (a,b, and c) and the underlying corrosion attack (d) for the sample exposed beneath a 2 µL 0.17 mM NaCl droplet exposed under paraffin oil for 24 h. The inserted SEM image in Figure 5(d) presents high magnification morphology of the region in Figure 5(d).

FIGURE 6. Two-dimensional (a) and three-dimensional (b) images of underlying corrosion attack formed under a 2 µL 0.17 mM NaCl droplet exposed under paraffin oil for 24 h. Corrosion products were removed using the ASTM G1-03 standard.

FIGURE 7. High magnification SEM SE images of the crystal structures in regions 1 (a, b, and c) and 2 (d, e, and f) of Figure 5(a).

FIGURE 8. Raman spectra of the corrosion products in regions 1 (a) and 2 (b) of Figure 5(a).

FIGURE 9. XPS high-resolution spectra of Fe 2p (a), O 1s (b), C 1s (c), and Cl 2p (d) of the corrosion products formed on the sample exposed with a 2 µL 0.17 mM NaCl droplet under paraffin oil for 24 h.

FIGURE 10. Calibration colors for the wide range pH indicator for various pH values (a−e). Images of the X100 pipeline steel samples exposed with the 2 µL 0.17 mM NaCl droplets under paraffin oil without (f) and with (g) the pH indicator for 1 h and without (h) and with (i) the pH indicator for 24 h.

FIGURE 11. Schematic model illustrating corrosion under a NaCl droplet for initial corrosion (≤ 1 h) (a) and longer term corrosion (24 h) (b) conditions.

TABLE CAPTIONS

TABLE 1. Chemical composition of the X100 pipeline steel samples.

TABLE 2. Raman spectra Peak positions corresponding to the crystalline corrosion products.

Figures

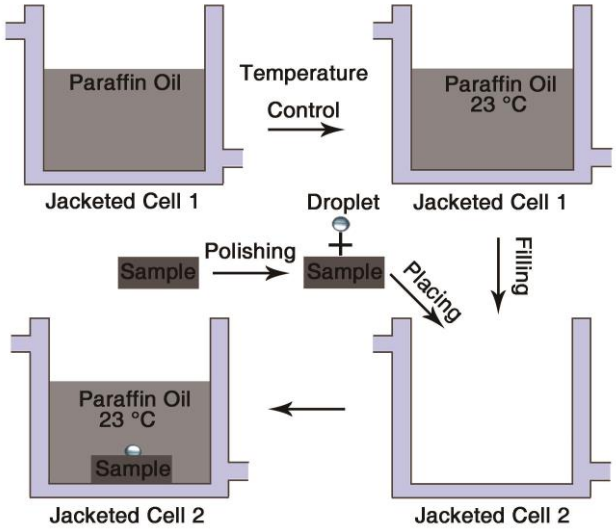

FIGURE 1. Schematic of the setup for droplet deposition and exposure under paraffin oil.

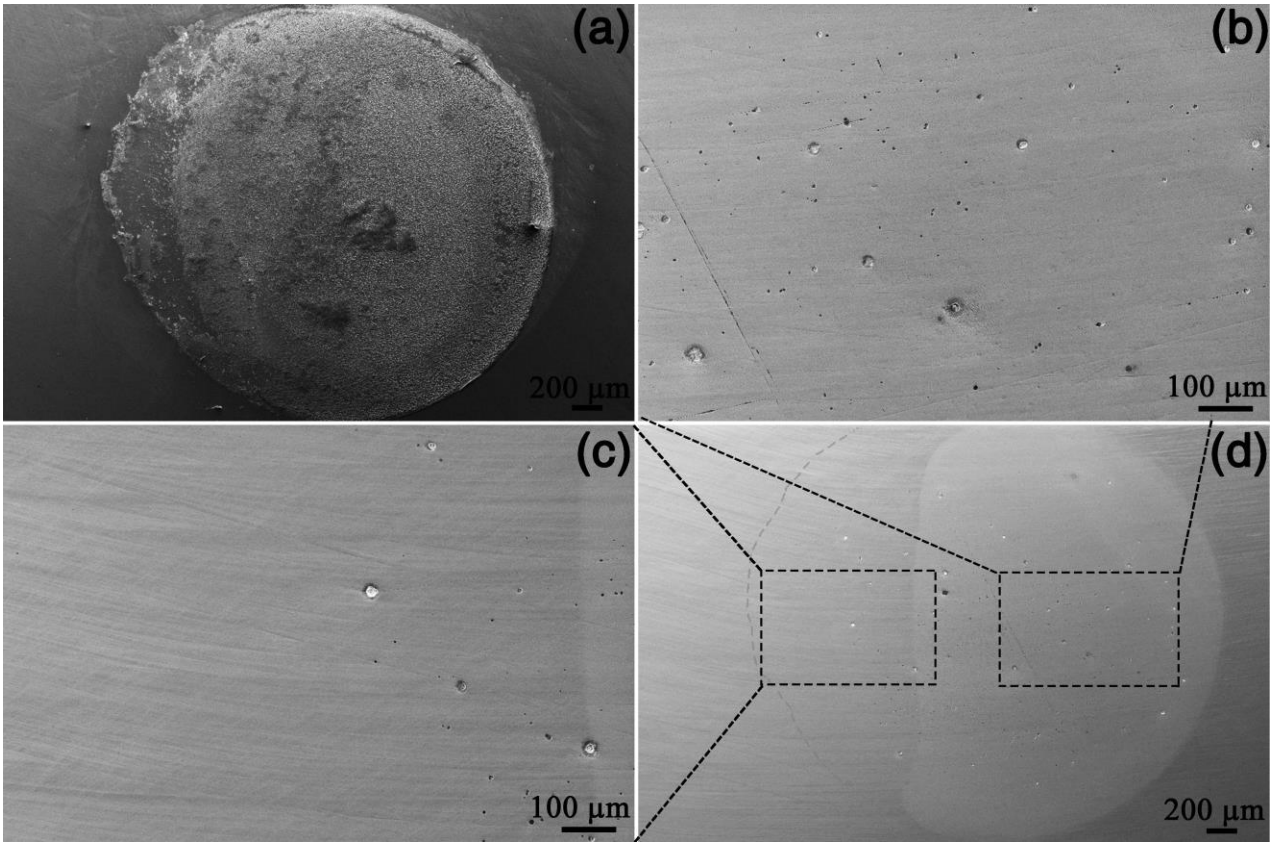

FIGURE 2. SEM secondary electron (SE) images of X100 pipeline steel specimen under a 2 µL 0.17 mM NaCl droplet beneath paraffin oil post 1 h exposure (a)and after removal of corrosion products (b, c, and d).

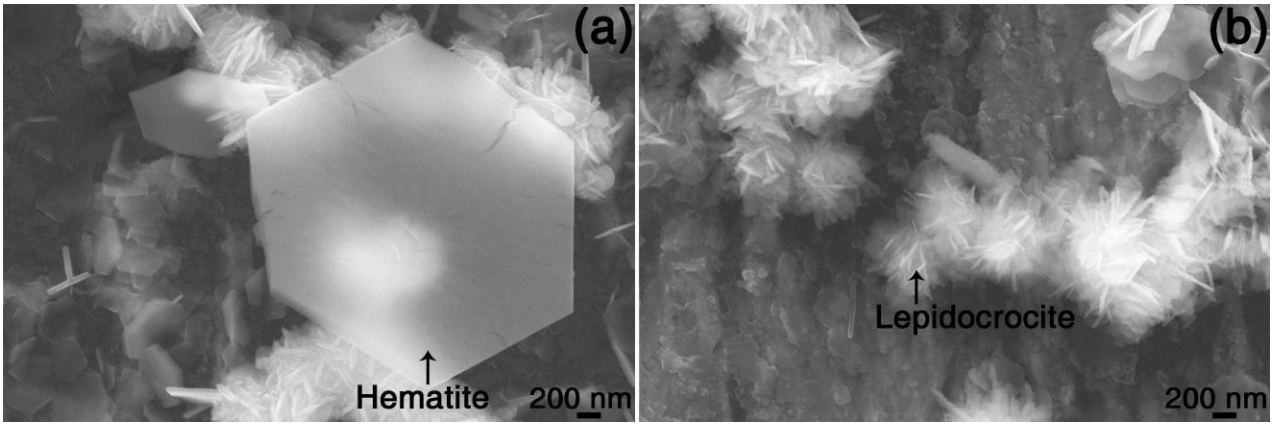

FIGURE 3. SEM SE images of the crystal structures of the corrosion products formed on the X100 pipeline steel specimen under a 2 µL 0.17 mM NaCl droplet exposed under paraffin oil for 1 h.

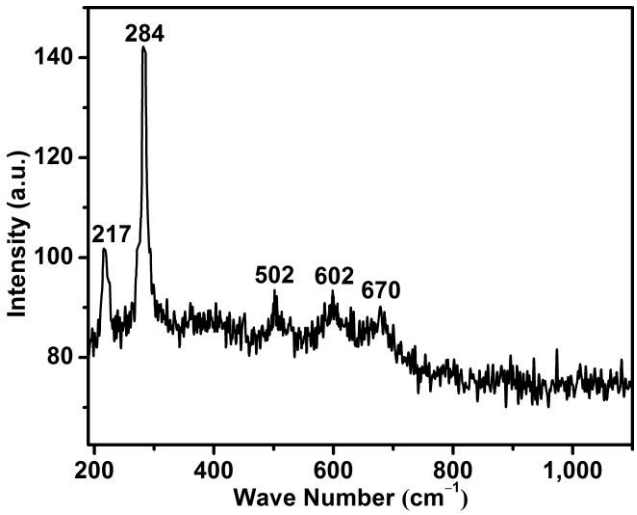

FIGURE 4. Raman spectrum of the corrosion products of the sample under a 2 µL 0.17 mM NaCl droplet exposed under paraffin oil for 1 h.

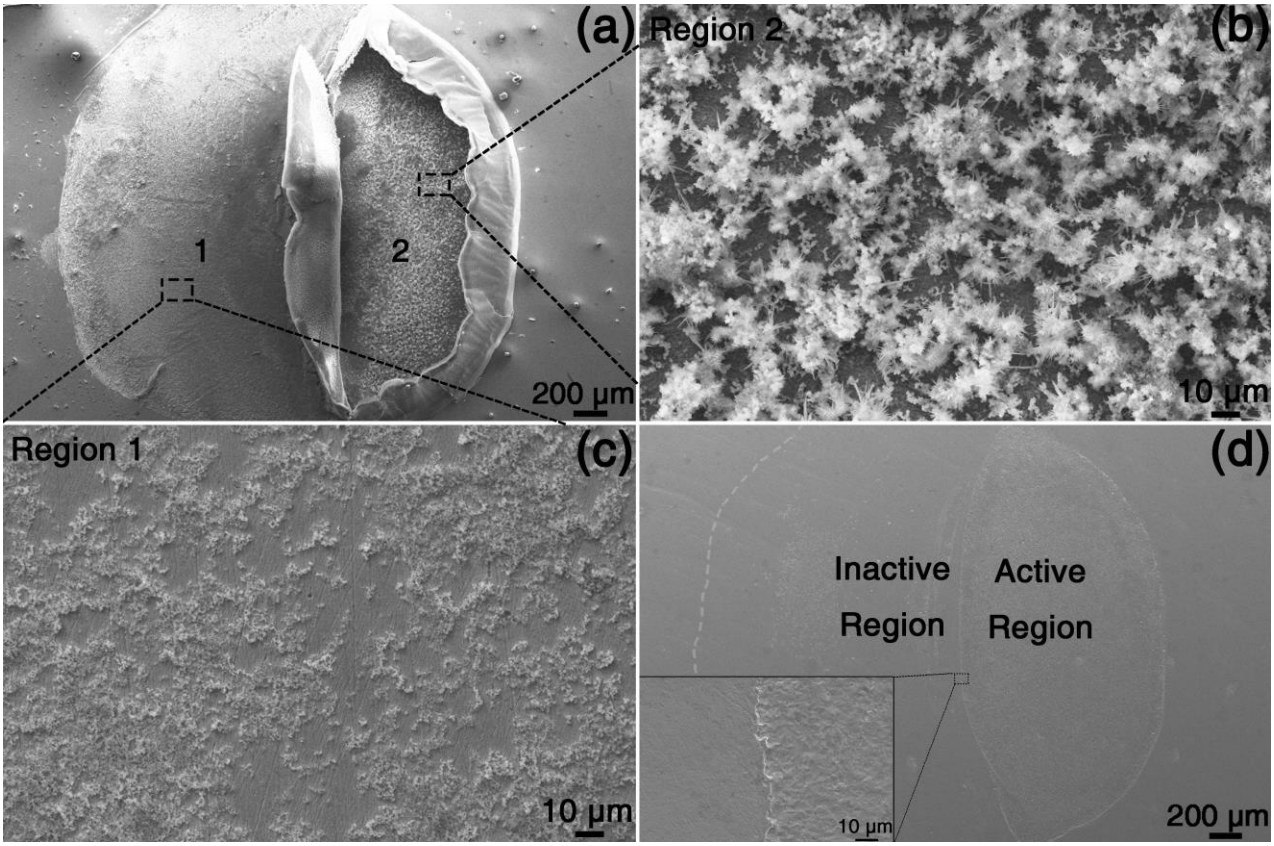

FIGURE 5. SEM SE images of the corrosion products (a,b, and c) and the underlying corrosion attack (d) for the sample exposed beneath a 2 µL 0.17 mM NaCl droplet exposed under paraffin oil for 24 h. The inserted SEM image in Figure 5(d) presents high magnification morphology of the region in Figure 5(d).

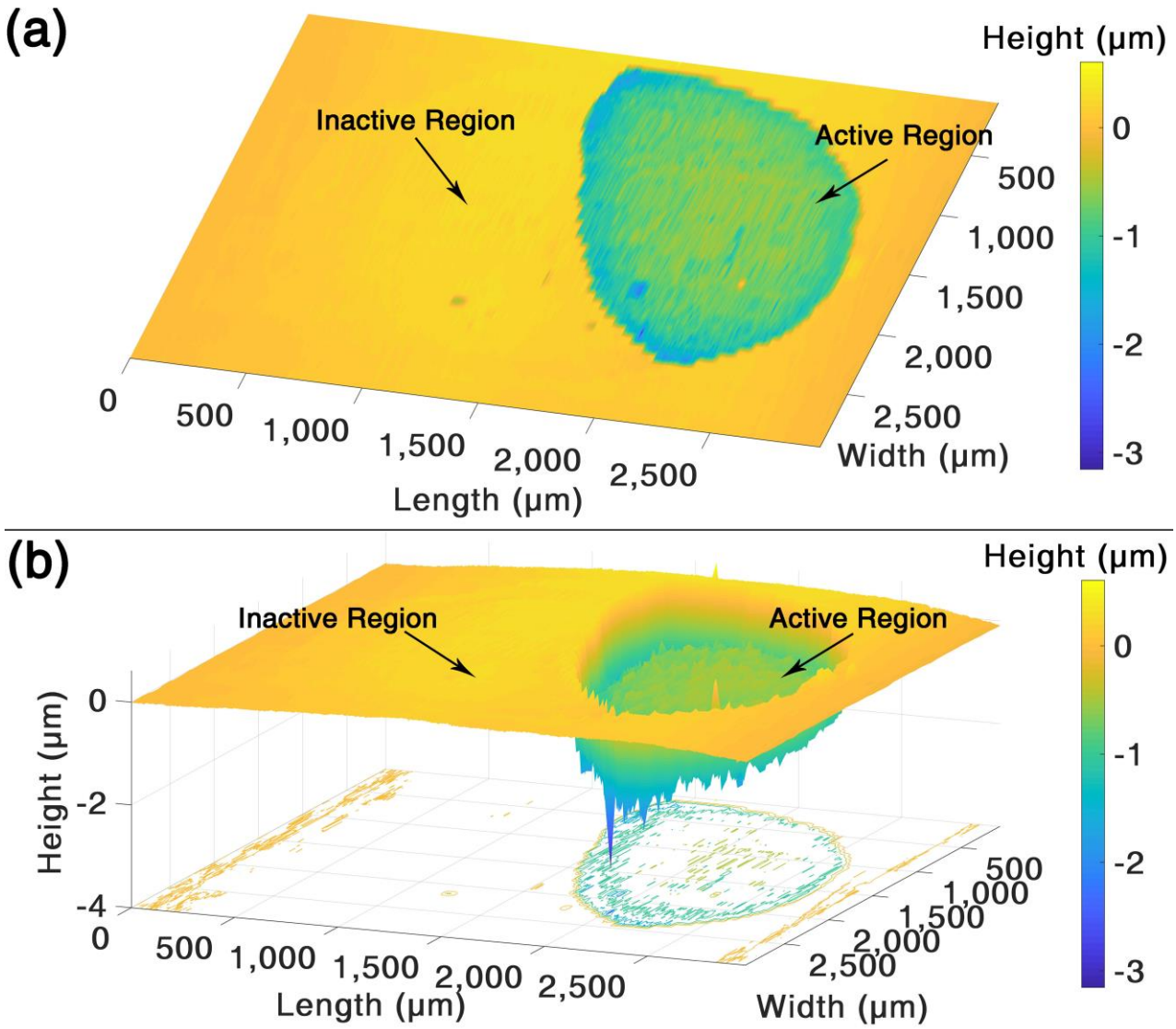

FIGURE 6. Two-dimensional (a) and three-dimensional (b) images of underlying corrosion attack formed under a 2 μL 0.17 mM NaCl droplet exposed under paraffin oil for 24 h. Corrosion products were removed using the ASTM G1-03 standard.

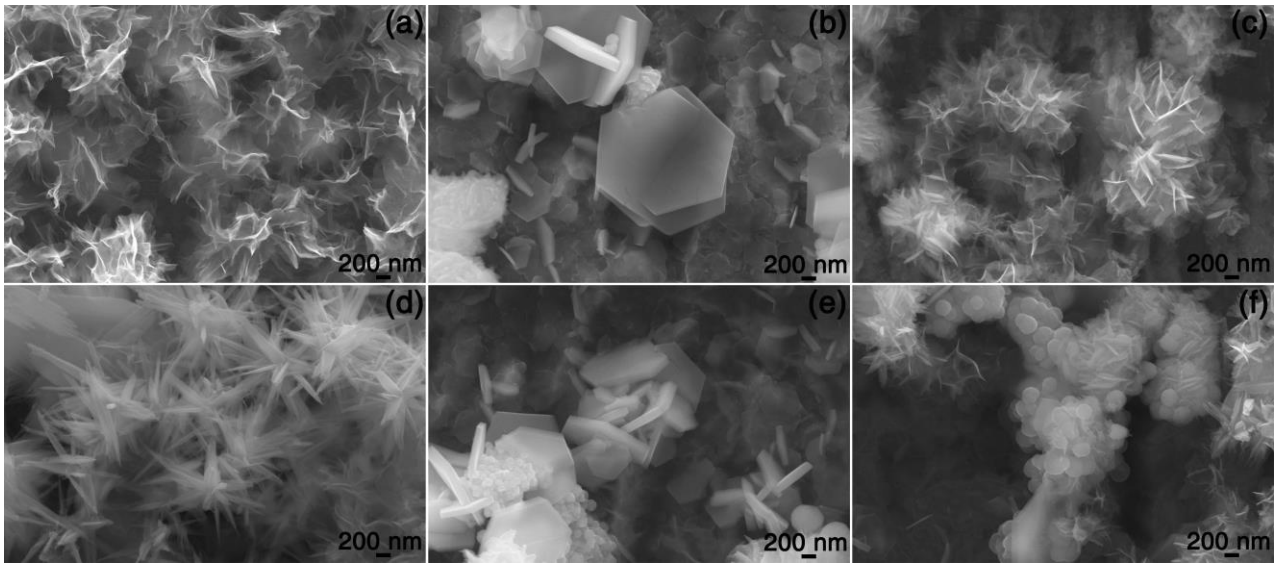

FIGURE 7. High magnification SEM SE images of the crystal structures in regions 1 (a, b, and c) and 2 (d, e, and f) of Figure 5(a).

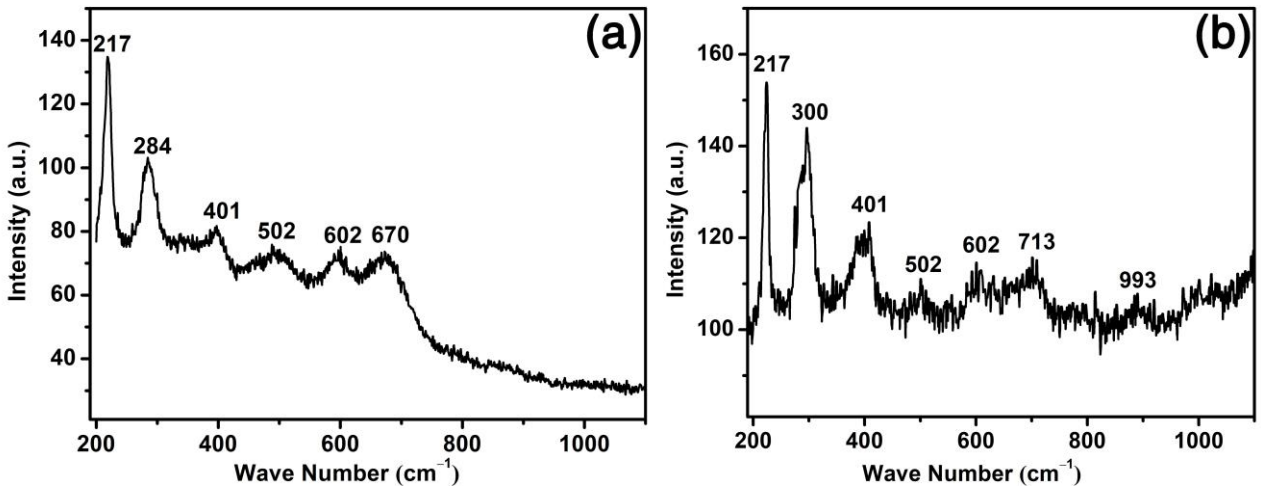

FIGURE 8. Raman spectra of the corrosion products in regions 1 (a) and 2 (b) of Figure 5(a).

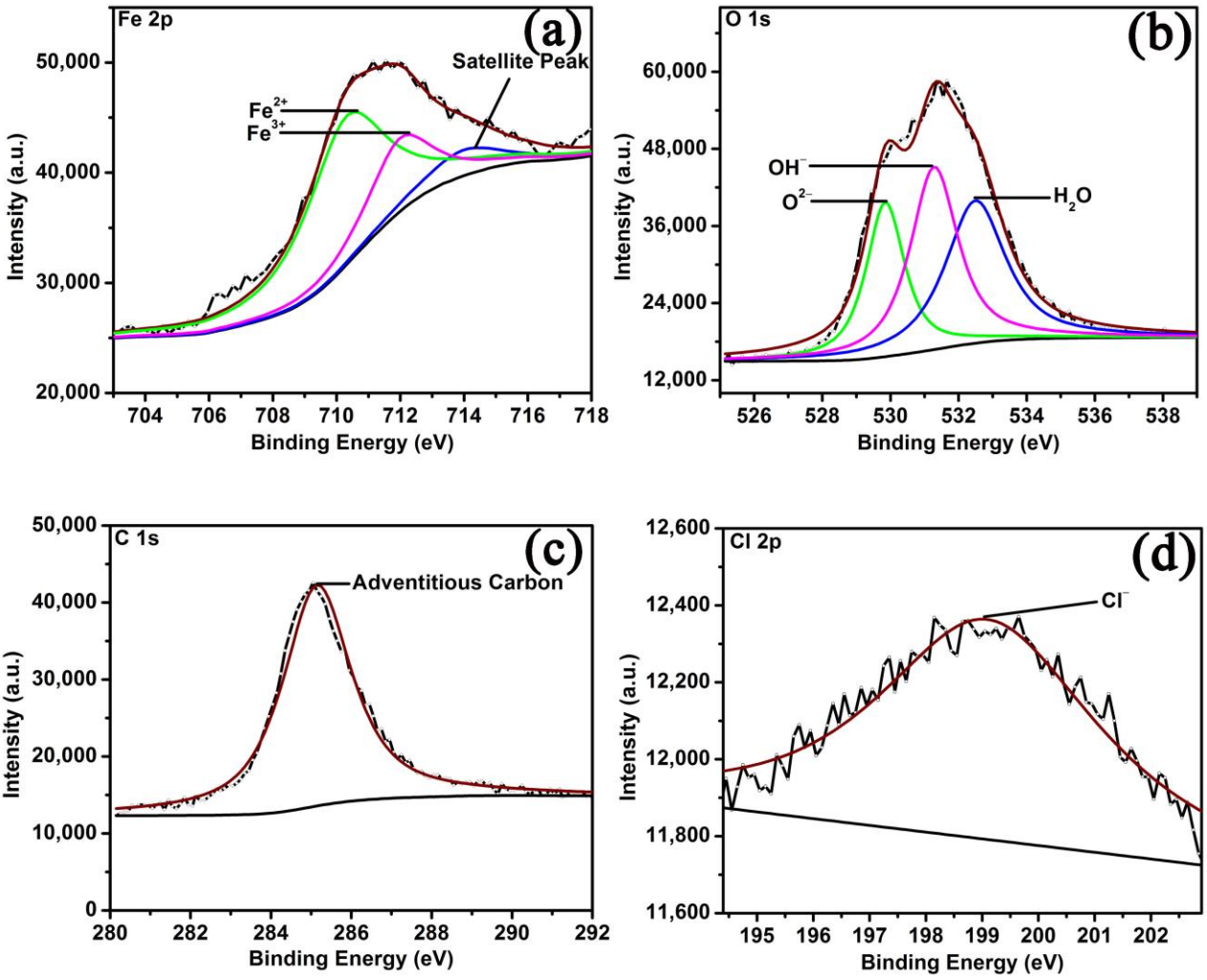

FIGURE 9. XPS high-resolution spectra of Fe 2p (a), O 1s (b), C 1s (c), and Cl 2p (d) of the corrosion products formed on the sample exposed with a 2 µL 0.17 mM NaCl droplet under paraffin oil for 24 h.

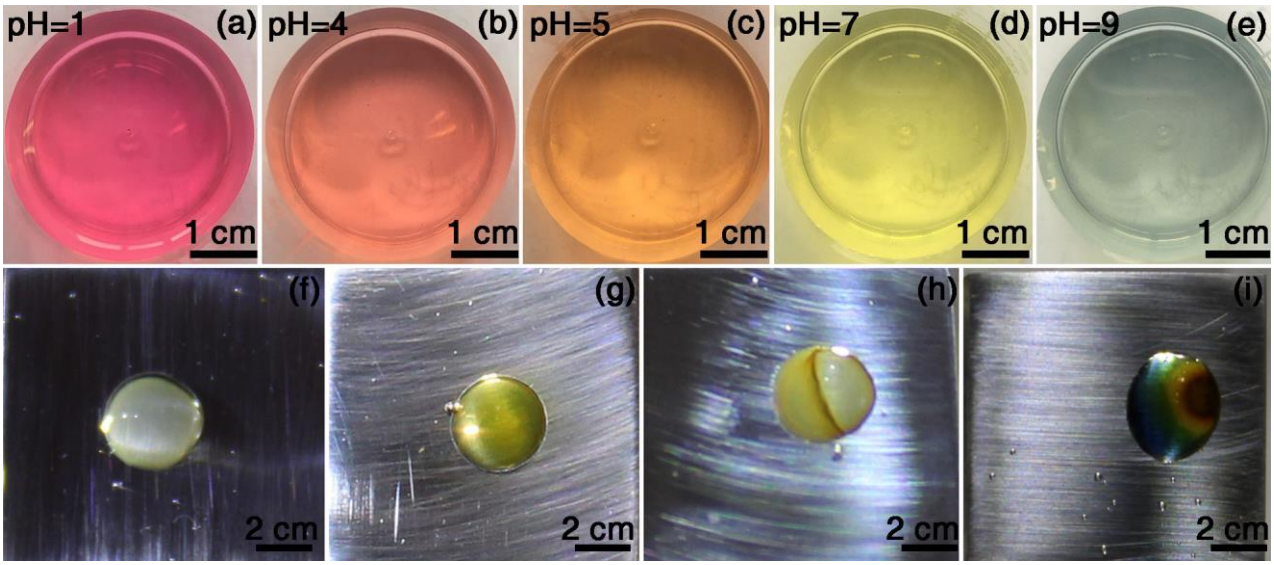

FIGURE 10. Calibration colors for the wide range pH indicator for various pH values (a–e). Images of the X100 pipeline steel samples exposed with the 2 µL 0.17 mM NaCl droplets under paraffin oil without (f) and with (g) the pH indicator for 1 h and without (h) and with (i) the pH indicator for 24 h.

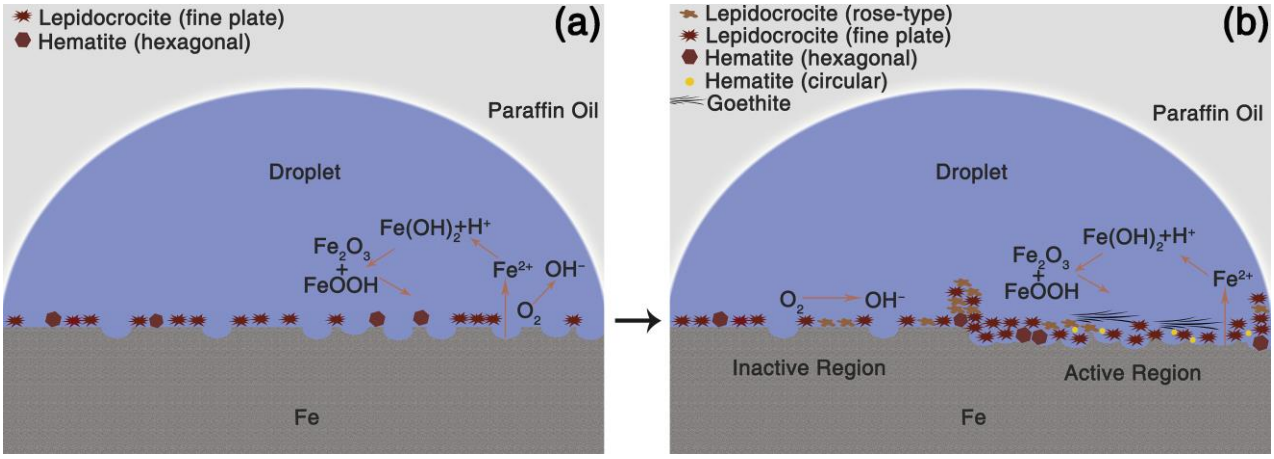

FIGURE 11. Schematic model illustrating corrosion under a NaCl droplet for initial corrosion (≤ 1 h) (a) and longer term corrosion (24 h) (b) conditions.

Tables

TABLE 1. Chemical composition of the X100 pipeline steel samples.

Element	C	Mo	Al	Mn	Cu	Ni	Ti	Cr	V	Nb
X100 (wt.%)	0.1	0.19	0.02	1.66	0.25	0.13	0.02	0.016	0.003	0.043

TABLE 2. Raman spectra peak positions corresponding to the crystalline corrosion products.

Crystal structure	Peak positions (cm^{-1})	References
Lepidocrocite	214, **245**, 301, 345, 373, 521, 644	[26]
	140, 214, 249, **284**, **345**, 374, **524**, 647	[24]
	166, 217, **251**, 310, 350, 378, 529, 655, 713, 1,300	[25]
	220, **250**, 309, 350, 377, 527, 648	[27]
Goethite	243, **300**, **388**, 417, 482, 553	[27]
	203, 244, 300, **387**, 399, 415, 480, 552, 684, 1,002, 1,113, 1,304	[25]
Hematite	**228**, 250, 294, 414, 502, 625, 670, 1,330	[25]
	228, 244, **296**, **413**, 497, 611, 659, 819	[27]
	220–228, 240–247, **289–299**, **400–415**, 497–502, 601–610, 1,320–1,330	[28]

The peak positions of the most prominent band in Raman spectra are in bold.